



Contents lists available at ScienceDirect

Solid-State Electronics

journal homepage: www.elsevier.com/locate/sse

Consistent low-field mobility modeling for advanced MOS devices

Zlatan Stanojević^{a,*}, Oskar Baumgartner^a, Lidija Filipović^a, Hans Kosina^a, Markus Karner^b, Christian Kernstock^b, Philipp Prause^b

^a Institute for Microelectronics, TU Wien, Gußhausstraße 27–29, 1040 Wien, Austria

^b Global TCAD Solutions GmbH, Landhausgasse 4/1a, 1010 Wien, Austria

ARTICLE INFO

Article history:

Available online xxxx

Keywords:

FinFET – Junction-less transistor
Surface roughness scattering
Linearized Boltzmann transport equation
Kubo–Greenwood transport formalism
Electron mobility
Semiconductor device simulation

ABSTRACT

In this paper we develop several extensions to semi-classical modeling of low-field mobility, which are necessary to treat planar and non-planar channel geometries on equal footing. We advance the state-of-the-art by generalizing the Prange–Nee model for surface roughness scattering to non-planar geometries, providing a fully numerical treatment of Coulomb scattering, and formulating the Kubo–Greenwood mobility model in a consistent, dimension-independent manner. These extensions allow meaningful comparison of planar and non-planar structures alike, and open the door to evaluating emerging device concepts, such as the FinFET or the junction-less transistor, on physical grounds.

© 2015 Elsevier Ltd. All rights reserved.

1. Introduction

A myriad of device architectures have been proposed to replace traditional MOS technologies, including planar architectures, such as ultra-thin body (UTB) devices, and non-planar ones, such as bulk-FinFETs [1,2] or SOI-FinFETs. Also, novel device ideas are emerging such as the junction-less FET [3]. In practice, one must be able to competitively rate different device designs and select the most appropriate one for the application at hand. Hence, a modeling framework able to perform these ratings consistently is highly desirable.

The low-field mobility is, strictly speaking, only valid for long-channel devices. However, it is directly related to the carrier mean free path and provides insight to the ballistics of the carriers for short-channel devices. Also, low-field mobility provides good insight into the transconductance characteristics of a device. It can be said that low-field mobility is a suitable *metric* for rating different device designs.

In this work we present a framework for low-field mobility modeling in planar and non-planar devices that is *consistent* and *dimension-independent*. As we are interested in the channel mobilities of nano-structured channels, the relevant system dimensionalities are (i) 1D cross-sections with 2D carrier gases, such as

MOS channels, and single-gate or double-gate UTB channels, and (ii) 2D cross-sections with 1D carrier gases, such as gate-all-around (GAA) or tri-gate channels.

The modeling framework is presented in the form of a *tool-chain* consisting of three parts, each dealing with a different physical aspect: (i) self-consistent Schrödinger–Poisson calculation for obtaining subband energies and wavefunctions, described in Section 2, (ii) scattering processes and their consistent extension to non-planar channels, laid out in Section 3, and (iii) low-field transport and mobility calculation, given in Section 4. In Section 5, we validate the consistency and dimension-independence, determine the critical dimension at which a channel develops 1DEG properties, and analyze two recently fabricated device designs.

All presented models were implemented within the Vienna Schrödinger–Poisson quantum simulator [4,5], available as part of GTS Framework [6].

2. Quantum confinement

In field effect transistors, planar or non-planar, carriers are confined to a conductive channel either by geometry, the electrostatic potential, or both. The effects of confinement are described by quantum mechanics and involve solving the Schrödinger equation.

For the sake of conciseness, we approximate the electronic structure of the channel using parabolic bands. However, the methods developed in this paper – especially the scattering models in Section 3 – are formulated in a generic manner, such that they

* Corresponding author.

E-mail addresses: stanojevic@iue.tuwien.ac.at (Z. Stanojević), baumgartner@iue.tuwien.ac.at (O. Baumgartner), lidija.filipovic@iue.tuwien.ac.at (L. Filipović), kosina@iue.tuwien.ac.at (H. Kosina), m.karner@globaltcad.com (M. Karner), c.kernstock@globaltcad.com (C. Kernstock), p.prause@globaltcad.com (P. Prause).

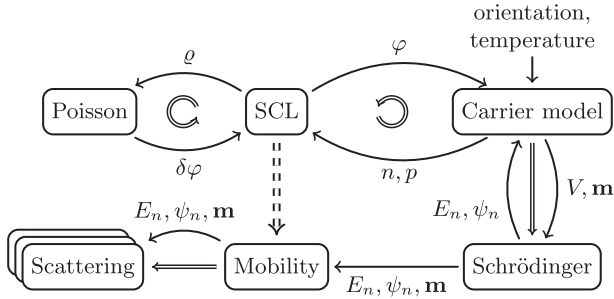


Fig. 1. Overall computational procedure; a self-consistent Schrödinger-Poisson loop (SCL) is run. The subband energies and wavefunctions of the converged solution are used to calculate scattering rates and mobilities. Single arrows represent data flow, double arrows control flow.

can be used with higher-order band structure models, such as $\mathbf{k}\cdot\mathbf{p}$ with little to no modification.

For parabolic bands, the effective mass Schrödinger equation

$$\frac{\hbar^2}{2} (\nabla \cdot \mathbf{m}^{-1} \cdot \nabla + V) \psi = E \psi, \quad (1)$$

is solved in the channel cross-section, where \mathbf{m} is the effective mass tensor. The tensor contains the anisotropy of the energy band and is transformed according to crystal orientation. Eq. (1) is discretized using a finite-volume scheme [5,7]; in the case of a 2D channel cross section a triangular mesh is used, and the finite-volume scheme accurately accounts for anisotropy in the cross-section plane.

The algebraic eigenvalue equation resulting from discretizing Eq. (1) is solved using the implicitly restarted Arnoldi method (IRAM) [8]. A large speedup of convergence is achieved using the shift-and-invert method [9]. Additionally, we devised an algorithm to compute eigenvalues in blocks, where for each block the IRAM solver is invoked. This allows to compute all eigenvalues λ of a system up to a certain threshold λ_{\max} [5]. This combination allows to process large geometries (>10 nm) with hundreds of subbands in a matter of seconds on a desktop computer.

The found energies and wavefunctions are used to calculate carrier concentrations and charge density. The latter affects the electrostatic potential via the Poisson equation. The coupled Schrödinger-Poisson system is solved self-consistently, as shown in Fig. 1.

3. Scattering

In this section we will focus on the scattering processes dominant in silicon nano-structures. These processes are non-polar phonon scattering, surface roughness scattering, and ionized impurity scattering. The same processes apply also to other elemental semiconductors, such as germanium. For compound semiconductors, such as GaAs, polar phonon scattering needs to be included, especially by polar LO-phonons. Alloy semiconductors, such as SiGe or InGaAs require alloy scattering to be included as well.

The starting point for each scattering process is Fermi's Golden Rule, which defines the transition rate

$$S_{n,n'}(\mathbf{k},\mathbf{k}') = \frac{2\pi}{\hbar} |H_{n,n';\mathbf{k},\mathbf{k}'}|^2 \delta(E(\mathbf{k}) - E(\mathbf{k}') \pm \hbar\omega), \quad (2)$$

from subband n to n' and from wavevector \mathbf{k} to \mathbf{k}' , through the square matrix element $|H_{n,n';\mathbf{k},\mathbf{k}'}|^2$. In the following sections we will review and extend the models for each of the three considered scattering processes to obtain a consistent set of models to be used for mobility calculation in Section 4.

3.1. Phonon scattering

Non-polar phonon scattering is divided into two types of processes: (i) scattering by acoustic phonons (acoustic deformation potential, ADP) and (ii) scattering by optical phonons (optical deformation potential, ODP, and inter-valley scattering, IVS). Scattering by acoustic phonons is considered quasi-elastic at room temperature and its square matrix element for 2DEG systems is given by [10]

$$|H_{n,n';\mathbf{k},\mathbf{k}'}|^2 = \frac{\pi k_B T D_A^2}{\hbar \rho_m v_l A} \int |\psi_{n,\mathbf{k}}(\mathbf{x})|^2 |\psi_{n',\mathbf{k}'}(\mathbf{x})|^2 d\mathbf{x}, \quad (3)$$

with the material parameters given in Table 1 and normalization area A . The integral is called the form-factor and is due to confinement. For 1DEG systems the formula in Eq. (3) is straightforwardly extended to [11]

$$|H_{n,n';\mathbf{k},\mathbf{k}'}|^2 = \frac{\pi k_B T D_A^2}{\hbar \rho_m v_l L} \int |\psi_{n,\mathbf{k}}(\mathbf{x},y)|^2 |\psi_{n',\mathbf{k}'}(\mathbf{x},y)|^2 dA, \quad (4)$$

with a normalization length L and again a form-factor integral. Both formulae can be written in a dimension-independent form,

$$|H_{n,n';\mathbf{k},\mathbf{k}'}|^2 = \frac{\pi k_B T D_A^2}{\hbar \rho_m v_l L^d} \int |\psi_{n,\mathbf{k}}(\mathbf{r})|^2 |\psi_{n',\mathbf{k}'}(\mathbf{r})|^2 d^{3-d}r, \quad (5)$$

where d is the dimension of the carrier gas. Since ADP scattering is considered quasi-elastic, $\hbar\omega$ is assumed to be zero.

Optical phonon scattering is treated analogously, giving the following dimension-independent expression for the square matrix element,

$$|H_{v,v';n,n';\mathbf{k},\mathbf{k}'}|^2 = \frac{(\hbar D_{v,v'})^2}{2\rho_m(\hbar\omega)L^d} \left(N + \frac{1}{2} \mp \frac{1}{2}\right) \int |\psi_{v,n,\mathbf{k}}(\mathbf{r})|^2 |\psi_{v',n',\mathbf{k}'}(\mathbf{r})|^2 d^{3-d}r, \quad (6)$$

for a transition from the state (n, \mathbf{k}) in valley v to (n', \mathbf{k}') in valley v' . For each branch of interacting phonons (longitudinal or transversal, acoustic or optical branches) different deformation potentials $D_{v,v'}$ and phonon energies $\hbar\omega$ are used.

3.2. Surface roughness scattering

Surface or interface roughness scattering (SRS) occurs at semiconductor surfaces, hetero-interfaces, and semiconductor-dielectric interfaces. Carriers scatter off the rough surface or interface which can be seen as a fluctuation of the interface's vertical position across the interface plane. SRS is elastic.

For 2D carrier gases the most widely used model for surface and interface roughness scattering was initially formulated by Prange and Nee [12]. Here, the square matrix element $|H_{n,n';\mathbf{k},\mathbf{k}'}|^2$ from Eq. (2) is effectively an average over an ensemble of rough channels, $\langle |H_{n,n';\mathbf{k},\mathbf{k}'}|^2 \rangle$. For a system of 2D carriers it reads

$$\langle |H_{n,n';\mathbf{k},\mathbf{k}'}|^2 \rangle = \frac{C(\mathbf{q})}{A} |F_{n,n';\mathbf{k},\mathbf{k}'}|^2, \quad (7)$$

where $\mathbf{q} = \mathbf{k} - \mathbf{k}'$, $C(\mathbf{q})$ is the roughness power spectrum, and $F_{n,n';\mathbf{k},\mathbf{k}'}$ are form-factors due to confinement. The form-factors account for the "closeness" of the states to the interface. They are commonly defined using the derivatives of the wavefunctions at the interface,

Table 1

Material parameters for acoustic phonon scattering and their values in silicon.

Quantity		Value in Si
D_A	deformation potential	14.6 eV
ρ_m	mass density	2.329 g/cm ³
c_l	sound velocity	9.04×10^3 m/s

$$F_{n,n';\mathbf{k},\mathbf{k}'} = \frac{\hbar^2}{2m} \frac{d\psi_{n,\mathbf{k}}^*}{dx} \frac{d\psi_{n',\mathbf{k}'}}{dx}. \quad (8)$$

Roughness is a random process and hence can only be characterized by its autocorrelation function $c(\mathbf{r}) = \langle \Delta(\mathbf{r})\Delta(\mathbf{r} + \mathbf{r}) \rangle$, where $\Delta(\mathbf{r})$ is the actual fluctuation of the interface position. The 2D-Fourier transform of the roughness autocorrelation function is the aforementioned roughness power spectrum. The autocorrelation function is frequently modeled either as Gaussian [12]

$$c(\mathbf{r}) = \Delta^2 e^{-\frac{r^2}{\Lambda^2}}, \quad C(\mathbf{q}) = \pi \Delta^2 \Lambda^2 e^{-\frac{q^2 \Lambda^2}{4}} \quad (9)$$

or exponential [13]

$$c(\mathbf{r}) = \Delta^2 e^{-\frac{\sqrt{2}r}{\Lambda}}, \quad C(\mathbf{q}) = \frac{\pi \Delta^2 \Lambda^2}{\left(1 + \frac{q^2 \Lambda^2}{2}\right)^{\frac{3}{2}}}. \quad (10)$$

The roughness amplitude Δ and autocorrelation length Λ are parameters of the rough surface or interface. In the frame of reference of a propagating electron, surface roughness appears as an ensemble of surface-bound acoustic phonons with a momentum distribution equal to $C(\mathbf{q})$.

The extension of SRS to 1DEG carriers is more involved than the extension procedure for phonon scattering. The reason for this is shown in Fig. 2. In a 2DEG the rough interface is always parallel with the direction of propagation. Wavefunctions are separated into a 1D standing wave perpendicular and a plane wave parallel to the interface. Hence, one only needs to be concerned with the plane wave part in the derivation of the SRS square matrix element, and the standing wave enters Eq. (7) only as a form-factor. In a 1DEG system, the wavefunctions are separated into a 2D standing wave in the channel cross section and a plane wave along the device axis. Now the roughness has to be taken into account not only in the plane-wave part but also in the standing wave part.

To evaluate the SRS matrix element $H_{n,n';\mathbf{k},\mathbf{k}'}$ for a 1DEG system, we start by taking a look at the perturbing potential in Fig. 3. The position of an abrupt potential step of height ΔV fluctuates by the value of function $\Delta(\mathbf{r})$. The resulting perturbing potential is either a very thin barrier or well (depending on the sign of $\Delta(\mathbf{r})$) of height ΔV and width $\Delta(\mathbf{r})$. We approximate the perturbing potential by

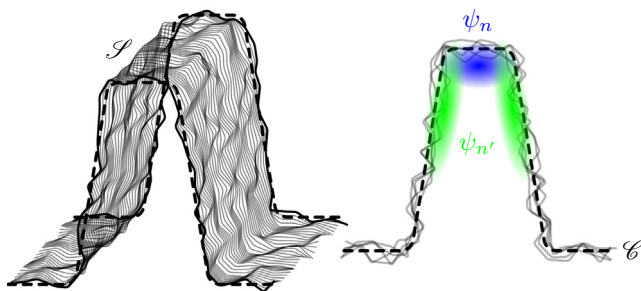
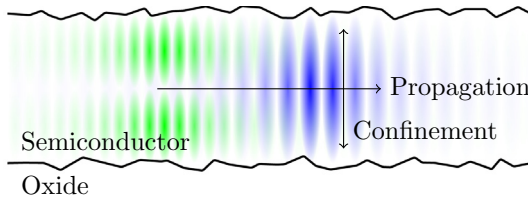


Fig. 2. Comparison of surface roughness scattering in a planar 2DEG (top) and a non-planar 1DEG (bottom) channel; in the 2DEG case the rough planes are parallel to the direction of free propagation in which the electronic state is described as plane wave. The initial and final states are selected via the plane-wave component only, resulting in $\mathbf{q} = \mathbf{k} - \mathbf{k}'$. In the 1DEG case roughness appears both along the axis and in the cross-section, thus both plane-wave and the standing wave component contribute to the state selection.

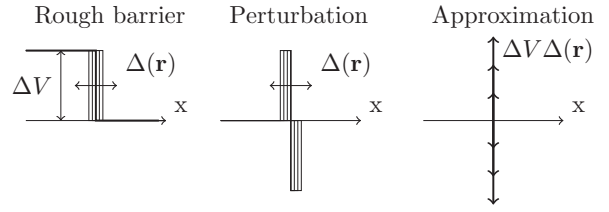


Fig. 3. The potential across the interface is modeled as a step function. The interface roughness causes the position of the abrupt potential step to fluctuate. Subtracting the potential of an ideal surface results in the perturbing potential which is either a thin barrier or a thin well depending in the sign of the fluctuation. For roughness amplitudes much smaller than the electron wavelength the thin barrier/well can be approximated as $\Delta V \Delta(\mathbf{r})$ -weighted δ -distribution.

a weighted surface-delta-distribution $\Delta V \Delta(\mathbf{r}) \delta(\mathbf{r} \in \mathcal{S})$, where \mathcal{S} represents the set of points on the ideal surface (Fig. 2). This allows us to convert the evaluation of the matrix element $H_{n,n';\mathbf{k},\mathbf{k}'}$ from a volume integration to a surface integration,

$$H_{n,n';\mathbf{k},\mathbf{k}'} = \Delta V \int_{\mathcal{S}} \Psi_{n,\mathbf{k}}^*(\mathbf{r}) \Psi_{n',\mathbf{k}'}(\mathbf{r}) \Delta(\mathbf{r}) dA. \quad (11)$$

This matrix element cannot be evaluated directly since $\Delta(\mathbf{r})$ is a random function. The ensemble average of the square magnitude of Eq. (11), however, can be evaluated:

$$\langle |H_{n,n';\mathbf{k},\mathbf{k}'}|^2 \rangle = \iint_{\mathcal{S}} dA dA' \Psi_{n,\mathbf{k}}^*(\mathbf{r}) \Psi_{n',\mathbf{k}'}(\mathbf{r}) \Psi_{n,\mathbf{k}}(\mathbf{r}') \Psi_{n',\mathbf{k}'}^*(\mathbf{r}') \Delta V^2 \langle \Delta(\mathbf{r}) \Delta(\mathbf{r}') \rangle. \quad (12)$$

So far we have made no assumptions about the electron states $\Psi_{n,\mathbf{k}}$. In a 1DEG system we separate the electron states into a two-dimensional bound state in the cross-section and a plane wave along the channel axis,

$$\Psi_{n,\mathbf{k}}(\mathbf{r}) = \psi_{n,\mathbf{k}}(\mathbf{r}) \frac{1}{\sqrt{L}} e^{ikz} = \psi_{n,\mathbf{k}}(x,y) \frac{1}{\sqrt{L}} e^{ikz}. \quad (13)$$

Using this separation approach, we can rewrite Eq. (12) as

$$\langle |H_{n,n';\mathbf{k},\mathbf{k}'}|^2 \rangle = \frac{1}{L^2} \iint_{\mathcal{S}} \iint_{\mathcal{S}'} f_{n,n';\mathbf{k},\mathbf{k}'}^*(s) f_{n,n';\mathbf{k},\mathbf{k}'}(s') e^{i(\mathbf{k}-\mathbf{k}') \cdot (\mathbf{z}-\mathbf{z}')} \langle \Delta(\mathbf{r}) \Delta(\mathbf{r}') \rangle dz dz' ds ds'. \quad (14)$$

The integration across surface \mathcal{S} was separated into integrations along curve \mathcal{C} , i.e. the intersection of \mathcal{S} with the cross-section plane, and a normalization length L along the channel direction; s denotes the path coordinate along the curve \mathcal{C} and z the axial coordinate. We introduced the form-functions $f_{n,n';\mathbf{k},\mathbf{k}'}(s)$ which are defined as

$$f_{n,n';\mathbf{k},\mathbf{k}'}(s) = \psi_{n,\mathbf{k}}^* \psi_{n',\mathbf{k}'} \Delta V. \quad (15)$$

The effect of different effective masses in the materials on either side of \mathcal{S} can be included in the form-functions as

$$f_{n,n';\mathbf{k},\mathbf{k}'}(s) = \psi_{n,\mathbf{k}}^* \psi_{n',\mathbf{k}'} (V_- - V_+) - \frac{\hbar^2}{2} \nabla \psi_{n,\mathbf{k};-}^* \cdot \mathbf{m}_-^{-1} \cdot \nabla \psi_{n',\mathbf{k}';-} + \frac{\hbar^2}{2} \nabla \psi_{n,\mathbf{k};+}^* \cdot \mathbf{m}_+^{-1} \cdot \nabla \psi_{n',\mathbf{k}';+}, \quad (16)$$

where the subscripts $+$ and $-$ indicate each side of \mathcal{S} . In the limit of high potential barriers (e.g. dielectrics), the wavefunctions $\psi_{n,\mathbf{k}}$ do not penetrate from one medium into the other but vanish at the interface. In that case the expression in Eq. (16) can be approximated by

$$f_{n,n';\mathbf{k},\mathbf{k}'}(\mathbf{r}) \approx \frac{\hbar^2}{2} \nabla \psi_{n,\mathbf{k}}^* \cdot \mathbf{m}_{\text{well}}^{-1} \cdot \nabla \psi_{n',\mathbf{k}'}. \quad (17)$$

Looking back at Eq. (14), we recall that $\langle \Delta(\mathbf{r}) \Delta(\mathbf{r}') \rangle = c(\mathbf{r})$ and represent the autocorrelation as inverse 2D Fourier transform of the roughness power spectrum,

$$c(\mathbf{r}) = \frac{1}{4\pi^2} \iint_{\mathbb{R}} C(\mathbf{q}) e^{iq_{\perp}(s-s')} e^{iq_{\parallel}(z-z')} dq_{\perp} dq_{\parallel}, \quad (18)$$

separating the roughness “wave vector” \mathbf{q} into an axial component q_{\parallel} and a component q_{\perp} along \mathcal{C} . Inserting Eq. (18) into Eq. (14), we arrive at

$$\langle |H_{n,n';\mathbf{k},\mathbf{k}'}|^2 \rangle = \frac{1}{4\pi^2 L^2} \iint_{\mathcal{C}} ds ds' \iint_{\mathbb{R}} dq_{\perp} dq_{\parallel} \int_0^L dz dz' f_{n,n';\mathbf{k},\mathbf{k}'}(s) \times f_{n,n';\mathbf{k},\mathbf{k}'}^*(s') C(\mathbf{q}) e^{iq_{\perp}(s-s')} e^{i(k-k'+q_{\parallel})(z-z')}. \quad (19)$$

Axial integration of the plane wave term $e^{i(k-k'+q_{\parallel})(z-z')}$ leads to a $2\pi L \delta(k-k'+q_{\parallel})$ expression thus simplifying the previous equation to

$$\langle |H_{n,n';\mathbf{k},\mathbf{k}'}|^2 \rangle = \frac{1}{2\pi L} \iint_{\mathcal{C}} ds ds' \int_{\mathbb{R}} dq_{\perp} f_{n,n';\mathbf{k},\mathbf{k}'}(s) f_{n,n';\mathbf{k},\mathbf{k}'}^*(s') C(\mathbf{q}) e^{iq_{\perp}(s-s')}. \quad (20)$$

A change of variables $s' - s =: s''$ gives

$$\langle |H_{n,n';\mathbf{k},\mathbf{k}'}|^2 \rangle = \frac{1}{2\pi L} \int_{\mathbb{R}} C(\mathbf{q}) dq_{\perp} \int_{\mathcal{C}} \left[\int_{\mathcal{C}} f_{n,n';\mathbf{k},\mathbf{k}'}(s) f_{n,n';\mathbf{k},\mathbf{k}'}^*(s+s'') ds \right] e^{iq_{\perp}s''} ds''. \quad (21)$$

The term in square brackets represents an autocorrelation of the form-functions $f_{n,n';\mathbf{k},\mathbf{k}'}(s)$ and the integration surrounding it is a Fourier transform $s \mapsto q_{\perp}$. Using the Wiener-Khinchin theorem we can express the Fourier transform of the autocorrelation of $f_{n,n';\mathbf{k},\mathbf{k}'}(s)$ as square magnitude of its Fourier transform $F_{n,n';\mathbf{k},\mathbf{k}'}(q_{\perp})$ obtaining the final expression for the square matrix element,

$$\langle |H_{n,n';\mathbf{k},\mathbf{k}'}|^2 \rangle = \frac{1}{2\pi L} \int_{\mathbb{R}} |F_{n,n';\mathbf{k},\mathbf{k}'}(q_{\perp})|^2 C(\mathbf{q}) dq_{\perp}. \quad (22)$$

A few assumptions are contained within this last step of our derivation: (i) For closed curves \mathcal{C} (e.g. a gate-all-around channel) the Fourier transform is in fact a Fourier series expansion. (ii) For open curves \mathcal{C} , such as the tri-gate channel in Fig. 2 the Fourier transform is effectively windowed by the finite length of the curve \mathcal{C} . However, due to electrostatic confinement the wavefunctions, the form functions decay exponentially towards both ends of \mathcal{C} . The windowing effect is therefore negligible. (iii) The roughness power spectrum is assumed to be isotropic, $C(\mathbf{q}) = C(q)$.

A computationally efficient procedure was devised to compute the spectral form-functions $F_{n,n';\mathbf{k},\mathbf{k}'}(q_{\perp})$ required for the integral in Eq. (22). The procedure is depicted in Fig. 4. The wavefunctions are used to compute the form-functions along the interface curve \mathcal{C} , which are resampled onto an equidistant q_{\perp} -grid and fast-Fourier-transformed to obtain their spectral counterparts $F_{n,n';\mathbf{k},\mathbf{k}'}(q_{\perp})$.

Having found the spectral form-functions $F_{n,n';\mathbf{k},\mathbf{k}'}(q_{\perp})$ the square matrix element in Eq. (22) is obtained via q_{\perp} -integration, visualized in Fig. 5. In the case of a parabolic subband structure the wavefunctions and thus the form-functions are independent of \mathbf{k} and \mathbf{k}' . So $F_{n,n';\mathbf{k},\mathbf{k}'}(q_{\perp}) = F_{n,n'}(q_{\perp})$ allows $|H_{n,n';\mathbf{k},\mathbf{k}'}|^2$ to be tabulated for different subband pairs n, n' and q_{\perp} -values further reducing computational cost.

The integral in Eq. (22) represents momentum conservation in the cross-section plane. We can summarize that in a planar geometry with 2DEG, carrier momentum conservation is characterized by a $\delta(\mathbf{k} - \mathbf{k}' + \mathbf{q})$ term. In a non-planar structure with a 1DEG, we still have a $\delta(k_{\parallel} - k'_{\parallel} + q_{\parallel})$ term for the axial direction. However, the cross-section momentum conservation is not sharply defined but is now accounted for by the integral in Eq. (22).

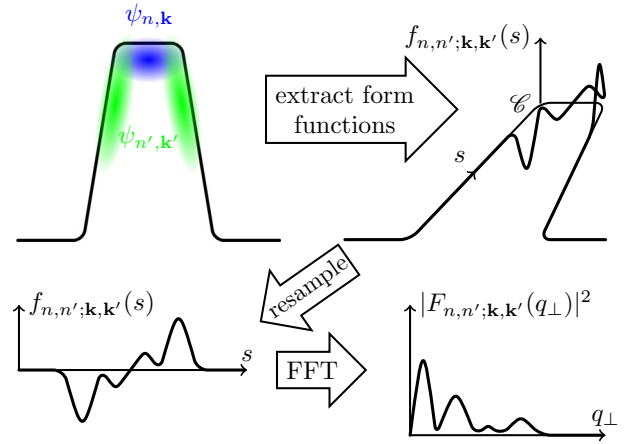


Fig. 4. Computational procedure to obtain the form-functions $f_{n,n';\mathbf{k},\mathbf{k}'}(s)$ and the spectral form-functions $F_{n,n';\mathbf{k},\mathbf{k}'}(q_{\perp})$: For each two cross-section wavefunctions $\psi_{n,\mathbf{k}}$ and $\psi_{n',\mathbf{k}'}$ the expression in Eq. (16) is evaluated along the interface curve \mathcal{C} on the mesh used for computing the states. The form-function $f_{n,n';\mathbf{k},\mathbf{k}'}(s)$ is interpolated onto an equidistant s -grid and padded with zeros if \mathcal{C} is open. The spectral form-function $F_{n,n';\mathbf{k},\mathbf{k}'}(q_{\perp})$ is computed using the fast Fourier transform (FFT) [14].

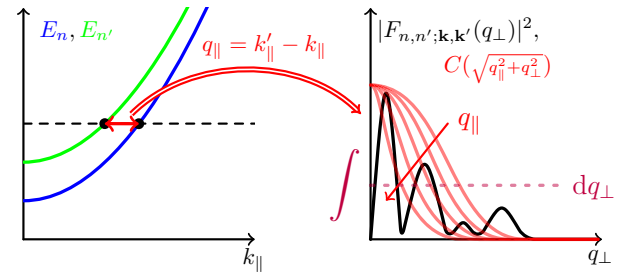


Fig. 5. Calculation of the square matrix element for a transition from subband n to subband n' in Eq. (22); for each energy value the difference of axial k -vectors is evaluated which represents the axial momentum transfer q_{\parallel} . The roughness power spectrum $C(q)$ is offset using $\sqrt{q_{\parallel}^2 + q_{\perp}^2}$ and its product with the spectral form-function $F_{n,n';\mathbf{k},\mathbf{k}'}(q_{\perp})$ integrated.

3.3. Ionized impurity scattering

Ionized impurity scattering (IIS) is of Coulomb type: The perturbing potential is due to the system's electrostatic response to a random charge distribution. The matrix element for an electrostatic potential φ is

$$H_{n,n';\mathbf{k},\mathbf{k}'} = -q_0 \int \Psi_{n,\mathbf{k}}^*(\mathbf{r}) \Psi_{n',\mathbf{k}'}(\mathbf{r}) \varphi(\mathbf{r}) dV, \quad (23)$$

where the electrostatic potential is determined by the Poisson equation

$$\nabla \cdot \epsilon \nabla \varphi + \varrho = 0. \quad (24)$$

For a random charge density ϱ , the potential φ is also a random function. Hence, Eq. (23) cannot be evaluated directly.

The relation between charge density and potential can be viewed as a filter. The potential is the low-pass filtered charge density, and the filter response is the electrostatic Green's function as shown in Fig. 6. Due to the $\mathbf{r} \leftrightarrow \mathbf{r}'$ -symmetry of the Green's function, the filter can be reversed and we can rewrite Eq. (23) as

$$\begin{aligned} H_{n,n';\mathbf{k},\mathbf{k}'} &= -q_0 \iint \Psi_{n,\mathbf{k}}^*(\mathbf{r}') \Psi_{n',\mathbf{k}'}(\mathbf{r}) G(\mathbf{r}, \mathbf{r}') \varrho(\mathbf{r}) dV dV' \\ &= - \int U_{n,n';\mathbf{k},\mathbf{k}'}(\mathbf{r}) \varrho(\mathbf{r}) dV, \end{aligned} \quad (25)$$

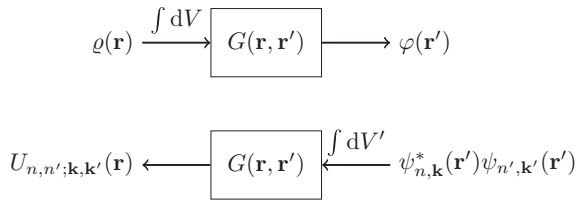


Fig. 6. The electrostatic problem viewed as a filter; the electrostatic Green's function can be applied to a charge density to obtain the potential. Conversely, the filter can be applied in reverse to the product of two wavefunctions to obtain a sensitivity function that maps the influence of a charge density onto the interaction's matrix element.

where we shall call the function

$$U_{n,n';k,k'}(\mathbf{r}) = q_0 \int \psi_{n,k}^*(\mathbf{r}') \psi_{n',k'}(\mathbf{r}') G(\mathbf{r}, \mathbf{r}') dV' \quad (26)$$

the *sensitivity function* of the interaction between state (n, \mathbf{k}) and (n', \mathbf{k}') due to a point charge at \mathbf{r} . The advantage of this approach is that $U_{n,n';k,k'}(\mathbf{r})$ can be easily computed numerically, as we will show.

Now we can evaluate the square matrix element. As with SRS, the square matrix element is in fact an ensemble average over channels with different random point charge distributions. We can write

$$\langle |H_{n,n';k,k'}|^2 \rangle = \iint U_{n,n';k,k'}^*(\mathbf{r}) U_{n,n';k,k'}(\mathbf{r}') \langle \rho(\mathbf{r}) \rho(\mathbf{r}') \rangle dV dV'. \quad (27)$$

If we assume that the point charge distributions in the ensemble are uncorrelated, $\langle \rho(\mathbf{r}) \rho(\mathbf{r}') \rangle \propto \delta(\mathbf{r}, \mathbf{r}')$, the square matrix element simplifies to

$$\langle |H_{n,n';k,k'}|^2 \rangle = q_0^2 \int |U_{n,n';k,k'}(\mathbf{r})|^2 N_{\text{imp}}(\mathbf{r}) dV, \quad (28)$$

where N_{imp} is the impurity concentration in the channel.

Now we will take a look at the *sensitivity function* from Eq. (26) and find ways to compute it efficiently. In a system with low-dimensional carriers we need to separate the cross-section coordinates where the confinement occurs (\mathbf{r}) and the coordinates of free propagation ($\mathbf{q} = \mathbf{k} - \mathbf{k}'$). After separation, the Poisson in the cross-section plane reads

$$[\nabla_{\perp} \cdot \varepsilon \nabla_{\perp} - \varepsilon q^2] \varphi_{\mathbf{q}}(\mathbf{r}) + \varrho_{\mathbf{q}}(\mathbf{r}) = 0. \quad (29)$$

The inverse of the operator in square brackets is the reduced Green's function $G_{\mathbf{q}}(\mathbf{r}, \mathbf{r}')$. The knowledge of the actual Green's function is not required, however. What is required is a way to compute the integral in Eq. (26) which is equivalent to solving the equation

$$[\nabla_{\perp} \cdot \varepsilon \nabla_{\perp} - \varepsilon \|\mathbf{k} - \mathbf{k}'\|^2] U_{n,n';k,k'}(\mathbf{r}) + q_0 \psi_{n,k}^*(\mathbf{r}) \psi_{n',k'}(\mathbf{r}) = 0, \quad (30)$$

to obtain the sensitivity function. The equation is readily discretized using finite volumes which also takes care of device geometry, interface conditions, and boundary conditions. The discretized system is solved using direct sparse methods [15]. For parabolic subband structures this has the benefit that the matrix of the discretized Eq. (30) needs to be factored only once for each $q = \|\mathbf{k} - \mathbf{k}'\|$ and only the much cheaper solve-step is applied for each wavefunction product $\psi_{n,k}^* \psi_{n',k'}$. As in the case of SRS, we can tabulate $|H_{n,n';k,k'}|^2$ for different subband pairs n, n' and q -values in order to reduce computational cost.

Screening in the linear approximation is included by adding an additional term to the Poisson equation,

$$[\nabla_{\perp} \cdot \varepsilon \nabla_{\perp} - \varepsilon q^2] \varphi_{\mathbf{q}}(\mathbf{r}) + \varrho_{\mathbf{q}}(\mathbf{r}) + \frac{d\varrho_{\mathbf{q}}}{d\varphi_{\mathbf{q}}} \varphi_{\mathbf{q}} = 0. \quad (31)$$

In general, evaluating the added term is not only computationally demanding, but it results in a full rather than sparse system when discretized, adding to the computational effort. Instead, we approximate screening in the static limit by a term resulting in a diagonal matrix [16], which for parabolic subbands reads

$$\frac{d\varrho_{\mathbf{q}}}{d\varphi_{\mathbf{q}}} = -q_0 \frac{dn_{\mathbf{q}}}{d\varphi_{\mathbf{q}}} \approx -q_0 \sum_n |\psi_n(\mathbf{r})|^2 N_{c,n}^d \mathcal{F}_{\frac{d}{2}-2} \left(\frac{E_n - E_F}{k_B T} \right) \frac{q_0}{k_B T}, \quad (32)$$

where $N_{c,n}^d$ is the effective density of states for a d -dimensional carrier gas [5], and \mathcal{F}_i is the complete Fermi–Dirac integral of order i .

4. Mobility calculation

This section is concerned with the procedure of computing the low-field mobility based on the scattering models given in the last section. A dimension-independent formulation of the problem will be elaborated and solutions will be derived that are applicable to both 2DEG and 1DEG systems without modification.

4.1. Current, conductivity, mobility

Low-field mobility is derived from the current equation,

$$\mathbf{J}_n = -\frac{q_0}{(2\pi)^d} \int_{\mathbb{R}^d} \mathbf{v}_n(\mathbf{k}) f_n^a(\mathbf{k}) d^d k, \quad (33)$$

where $\mathbf{v}_n(\mathbf{k})$ denotes the group velocity and f^a the asymmetric part of the distribution function f . For low driving fields, the asymmetric part is approximated as the linear distribution response f^1 with respect to the field \mathbf{E} . It is convenient to express \mathbf{J} as a linear function of \mathbf{E} since it allows one to extract the conductivity from $\mathbf{J} = \sigma \cdot \mathbf{E}$. To facilitate this, a microscopic relaxation time τ [17] is introduced, such that

$$f_n^1(\mathbf{k}) = q_0 \mathbf{v}_n(\mathbf{k}) \cdot \boldsymbol{\tau}_n(\mathbf{k}) \cdot \mathbf{E} \frac{df^0}{dE}, \quad (34)$$

with f^0 denoting the equilibrium Fermi–Dirac distribution. Inserting Eq. (34) into Eq. (33), the conductivity can be obtained:

$$\sigma_n = -\frac{q_0^2}{(2\pi)^d} \int_{\mathbb{R}^d} \mathbf{v}_n(\mathbf{k}) \otimes \mathbf{v}_n(\mathbf{k}) \tau_n(\mathbf{k}) \frac{df^0}{dE} d^d k. \quad (35)$$

For parabolic bands, the integration over \mathbf{k} is replaced by an integration over energy to obtain

$$\sigma_n = -q_0^2 \mathbf{m}_n^{-1} \cdot \frac{2}{d} \int_0^\infty \tau_n(E) \frac{\partial f^0}{\partial E} E g_n^d(E) dE, \quad (36)$$

using the d -dimensional density of states $g_n^d(E)$. Note that the relaxation time in both Eqs. (34) and (36) is a tensor. This is necessary to correctly account for anisotropic scattering processes, such as Coulomb scattering or surface-roughness scattering, which prefer small deflections between initial and final momenta as illustrated in Fig. 7. Due to symmetry, the tensors \mathbf{m} and $\boldsymbol{\tau}_n(E)$ have the same principal directions, which implies that they commute. The expression in Eq. (36) can be separated into principal components,

$$\sigma_{n,\xi} = -q_0^2 \frac{1}{m_{n,\xi}} \cdot \frac{2}{d} \int_0^\infty \tau_{n,\xi}(E) \frac{\partial f^0}{\partial E} E g_n^d(E) dE, \quad (37)$$

where ξ denotes each principal direction. Finally, subband mobility μ_n and total mobility μ are computed as

$$\mu_n = \frac{\sigma_n}{q_0 n_n}, \quad \mu = \frac{1}{q_0 n} \sum_n \sigma_n. \quad (38)$$

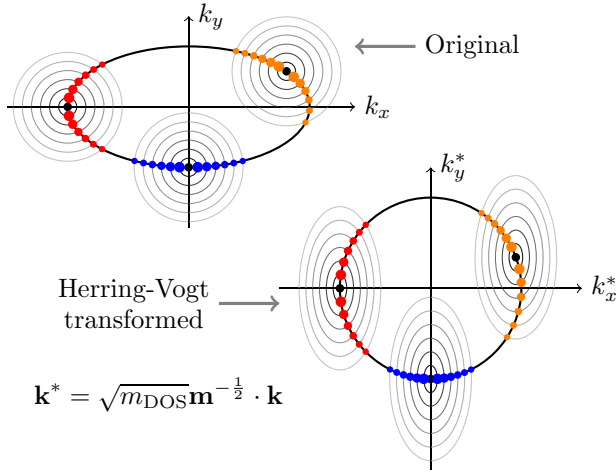


Fig. 7. Band anisotropy and scattering anisotropy; different positions of the initial state in \mathbf{k} -space result in different probability distributions of final states. Applying a Herring-Vogt transform eliminates band anisotropy but distorts the \mathbf{q} -dependence of the scattering process at the same time. In both cases the relaxation time can only be described as a tensor.

4.2. Linearized Boltzmann equation

The linear distribution response f^1 is governed by the linearized Boltzmann transport equation (LBTE), which for elastic scattering processes reads

$$\sum_{n', \mathbf{k}'} S_{n, n'}(\mathbf{k}, \mathbf{k}') [f_n^1(\mathbf{k}) - f_{n'}^1(\mathbf{k}')] = q_0 \mathbf{E} \cdot \mathbf{v}_n(\mathbf{k}) \frac{df^0}{dE}. \quad (39)$$

Inserting Eq. (34), we obtain an equation for the microscopic relaxation time,

$$\sum_{n', \mathbf{k}'} S_{n, n'}(\mathbf{k}, \mathbf{k}') [\mathbf{v}_n(\mathbf{k}) \cdot \boldsymbol{\tau}_n(\mathbf{k}) \cdot \mathbf{E} - \mathbf{v}_{n'}(\mathbf{k}') \cdot \boldsymbol{\tau}_{n'}(\mathbf{k}') \cdot \mathbf{E}] = \mathbf{v}_n(\mathbf{k}) \cdot \mathbf{E}. \quad (40)$$

Fortunately, for parabolic bands, the different principal components τ_ξ are not coupled by Eq. (40), so we can write

$$\sum_{n', \mathbf{k}'} S_{n, n'}(\mathbf{k}, \mathbf{k}') \left[\tau_{n, \xi}(E) \frac{\hbar k_\xi}{m_{n, \xi}} - \tau_{n', \xi}(E) \frac{\hbar k'_\xi}{m_{n', \xi}} \right] = \frac{\hbar k_\xi}{m_{n, \xi}} \quad (41)$$

for each principal direction ξ . k_ξ denotes the projection of \mathbf{k} along principal direction ξ . We recall from Eq. (2) that for elastic processes $S_{n, n'}(\mathbf{k}, \mathbf{k}') = \frac{2\pi}{\hbar} |H_{n, n'; \mathbf{k}, \mathbf{k}'}|^2 \delta(E(\mathbf{k}) - E(\mathbf{k}'))$ which decouples Eq. (41) for different energies. Since $\tau_{n, \xi}$ itself depends on the energy but not the direction of \mathbf{k} , a system of equations can be formulated for every energy as

$$L_n \tau_{n, \xi} - M_{n, n'} \tau_{n', \xi} = 1, \quad (42)$$

where the coefficients are

$$L_n = \sum_{n'} g_{n'}^d(E) J_{n, n', \xi}, \quad (43)$$

$$M_n = g_n^d(E) \sqrt{\frac{m_{n, \xi}(E - E_n)}{m_{n', \xi}(E - E_{n'})}} J'_{n, n', \xi}. \quad (44)$$

The integrals $J_{n, n', \xi}$ and $J'_{n, n', \xi}$ are defined as

$$J_{n, n', \xi} = \frac{d}{\Omega_d^2} \int_{\Omega_d \times \Omega_d} \frac{\pi}{\hbar} |H_{n, n'; \mathbf{k}, \mathbf{k}'}|^2 \cos^2 \vartheta_\xi d\Omega'_d d\Omega_d, \quad (45)$$

$$J'_{n, n', \xi} = \frac{d}{\Omega_d^2} \int_{\Omega_d \times \Omega_d} \frac{\pi}{\hbar} |H_{n, n'; \mathbf{k}, \mathbf{k}'}|^2 \cos \vartheta_\xi \cos \vartheta'_\xi d\Omega'_d d\Omega_d, \quad (46)$$

with ϑ_ξ denoting the angle between the Herring-Vogt transformed [18] vector \mathbf{k}^* and the principal direction ξ ,

$$\cos \vartheta_\xi = \frac{\mathbf{k}^* \cdot \mathbf{e}_\xi}{k^*}. \quad (47)$$

Ω_d denotes the surface of d -dimensional “unit sphere” which measures 2 for 1DEG and 2π for 2DEG. The integrals in Eqs. (45) and (46) can be understood as

$$\int_{\Omega_d \times \Omega_d} f(\vartheta, \vartheta') d\Omega'_d d\Omega_d = \begin{cases} f(0, 0) + f(0, \pi) + f(\pi, 0) + f(\pi, \pi) & : 1\text{DEG} \\ \int_0^{2\pi} \int_0^{2\pi} f(\vartheta, \vartheta') d\vartheta d\vartheta' & : 2\text{DEG}. \end{cases} \quad (48)$$

Inelastic phonon-scattering is isotropic, and $M_{n, n'}$ vanishes in that case. To account for the energy relaxation, $L_n \tau_{n, \xi}$ needs to be weighted by

$$\frac{(1 - f^0(E \pm \hbar\omega)) g_n^d(E \pm \hbar\omega)}{(1 - f^0(E)) g_n^d(E)}. \quad (49)$$

Eq. (42) represents a system of equations the rank of which is equal to the number of subbands intersecting energy E . It is a small dense system and can be readily solved using direct methods.

5. Results

In this section we will first validate the consistency of the developed modeling framework between the 2DEG and 1DEG cases. Then, a critical length will be established, below which electrons in silicon exhibit 1DEG properties. Finally, we will employ the modeling framework to evaluate two recently realized device designs, the bulk FinFET [1], and the junction-less nanowire FET [3].

5.1. Validation

As we derived the models for carrier confinement, scattering, and mobility in a consistent, dimension-independent way for both 2DEG and 1DEG systems, we should expect computed mobilities to be consistent as well. To test this, we chose the simulation setup shown in Fig. 8. For a wide channel (60 nm) the mobilities computed from the 1DEG system and the 2DEG system of the vertical cut through the stack should coincide. This is indeed the case as shown in Figs. 9 and 10 for substrate/channel-orientations $\{100\}/\langle 100 \rangle$ and $\{110\}/\langle 100 \rangle$.

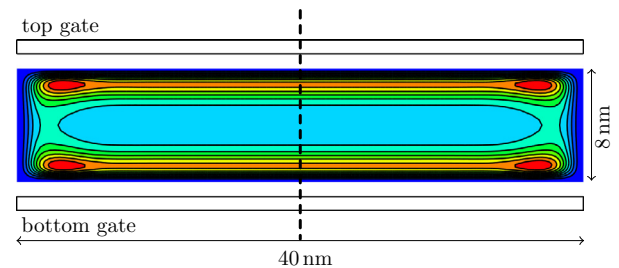


Fig. 8. Simulation setup used for validating the consistency between 2DEG and 1DEG simulations; a finite-width double-gate silicon UTB MOS is simulated as 2D cross-section and the mobility of the 1DEG is extracted; colors indicate the electron concentration from this simulation. The same device is cut along the dashed line, the simulation is performed for a 1D cross-section and mobility is obtained for the 2DEG. (For interpretation of the references to colour in this figure legend, the reader is referred to the web version of this article.)

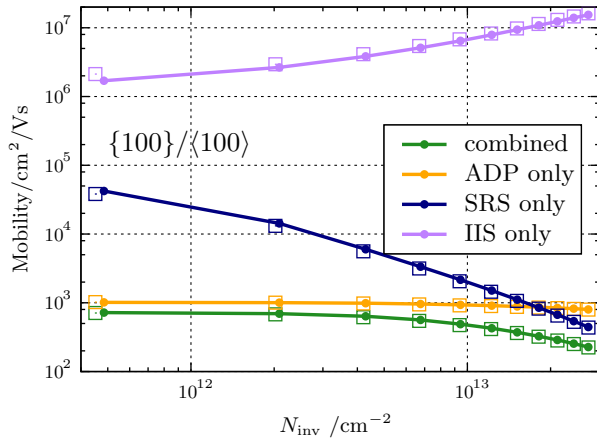


Fig. 9. Comparison between 2DEG mobility (solid lines) and 1DEG mobility (open symbols) for a 40 nm wide silicon UTB MOS; substrate and channel have {100}/⟨100⟩-orientation.

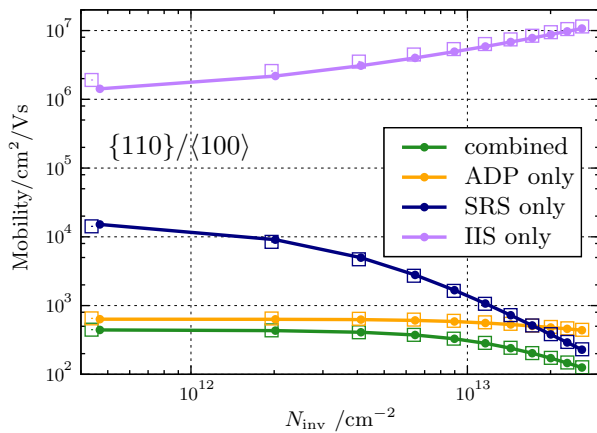


Fig. 10. Same as Fig. 9 for a {110}/⟨100⟩-oriented channel.

5.2. Critical width

We can now ask the question what the *critical width* is, at which the 1DEG mobilities start to diverge from 2DEG. This was investigated by simulating an ensemble of finite-width UTB channels ranging from 10 nm to 60 nm in steps of 2 nm.

We first have a look at the inversion density versus gate voltage for {100}/⟨100⟩-oriented channels in Fig. 11. Here the curves of all but the first two widths match the 2DEG limit. We can conclude that the critical dimension for electron inversion density in silicon is $L_{crit} \approx 12$ nm.

If we now look at the mobility curves in Fig. 12, we observe a different behavior. Here, the convergence towards the 2DEG limit with increasing width happens much slower than for the inversion density which is mostly due to SRS dependence on device width. Here, the critical dimension is about twice as large, $L_{crit} \approx 24$ nm. The critical dimension, however, depends on orientation, temperature, carrier type, and material, and a different value might be found for channels that are p-type, have different orientations, or contain other materials.

The conclusion we can draw here is that for channel cross sections approaching feature sizes of L_{crit} the 2DEG picture starts losing validity and a 2D model for confinement combined with a 1DEG model for transport is needed. This is especially important when considering tri-gate devices where one might be tempted to treat each Si/SiO₂ interface as an independent 2DEG system.

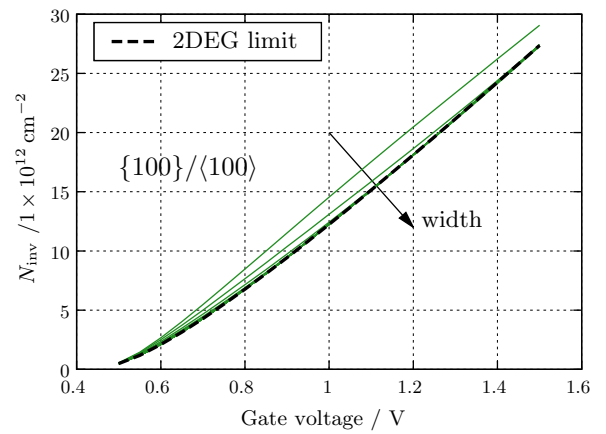


Fig. 11. The inversion density converges quickly towards the 2DEG limit with only the first two curves (10 nm and 12 nm widths) showing any noticeable discrepancy.

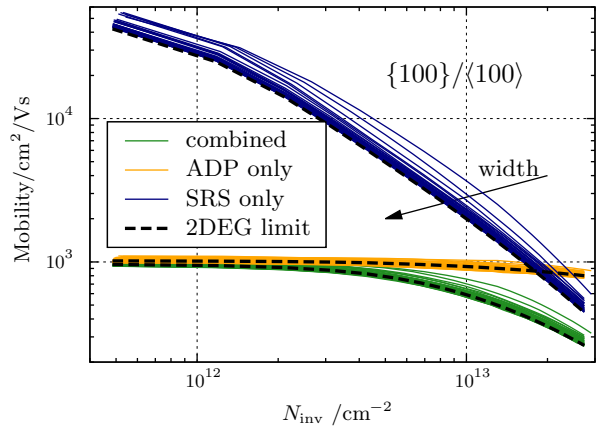


Fig. 12. Mobility converges much slower towards the 2DEG limit than the inversion density shown in Fig. 11. The width dependence is most pronounced in SRS.

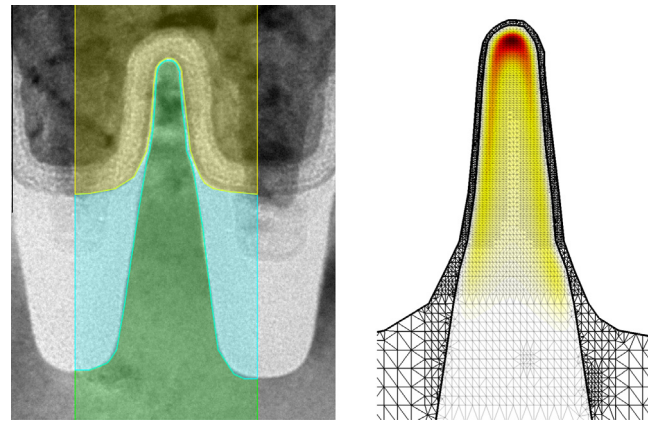


Fig. 13. Left: TEM image of a tri-gate channel cross-section fabricated by Intel [1]; segments of the computational domain are shown in color [6]. Right: Computed self-consistent electron concentration for a [110]/⟨001⟩ channel/substrate orientation. The computational grid is visible as well. (For interpretation of the references to color in this figure legend, the reader is referred to the web version of this article.)

Such an approach would lose validity as soon as characteristic sizes approach L_{crit} . Note that due to electrostatic confinement the actual characteristic sizes may be even below the ones given by geometry.

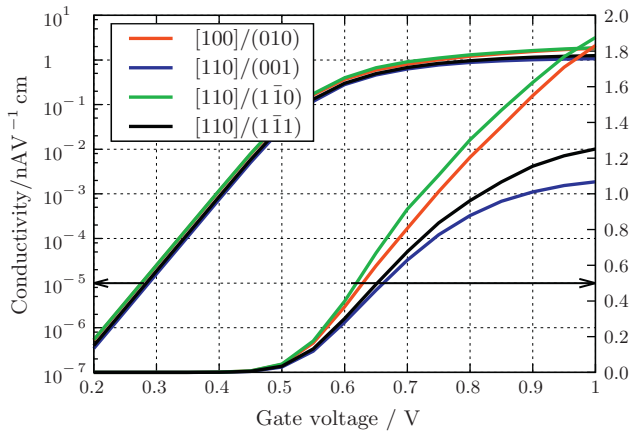


Fig. 14. Channel conductivity vs. gate voltage for the device shown in Fig. 13; Different channel/substrate orientations show different behavior due to orientation-dependence of SRS.

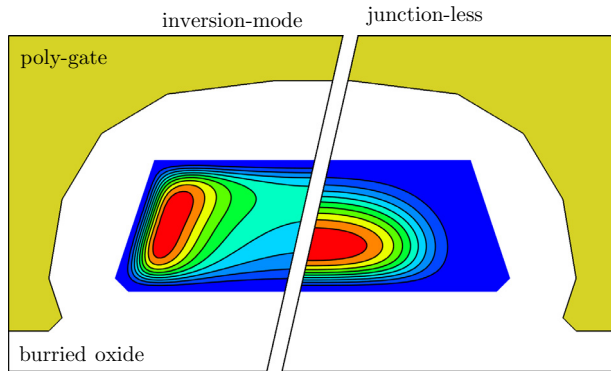


Fig. 15. Electron concentration in a pi-gate channel cross-section; left – inversion-mode device, right – junction-less device; both devices are biased above threshold. In the inversion-mode FET electrons are pushed towards the top and sidewalls while in the junction-less FET electrons remain centered.

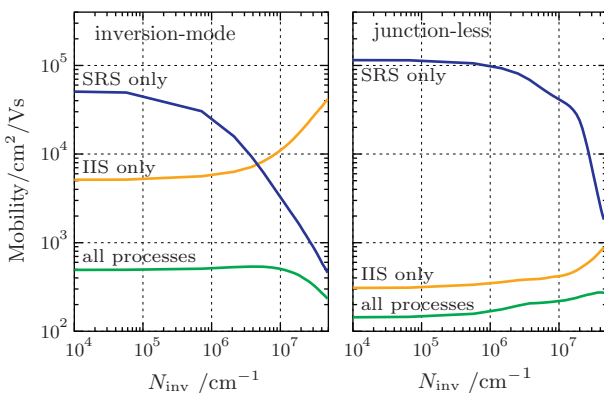


Fig. 16. Mobility curves for channel from Fig. 15; left – inversion-mode device, right – junction-less device; the dominant scattering processes are reversed for the two device types. In inversion-mode channels IIS is negligible and SRS dominates when the device is switched on. In the junction-less FET IIS is stronger by an order of magnitude, limiting the mobility, while SRS becomes effective at high densities only.

5.3. Realistic device cross-sections

Having developed and verified our modeling framework we can now turn our attention to more realistic device cross-sections. One

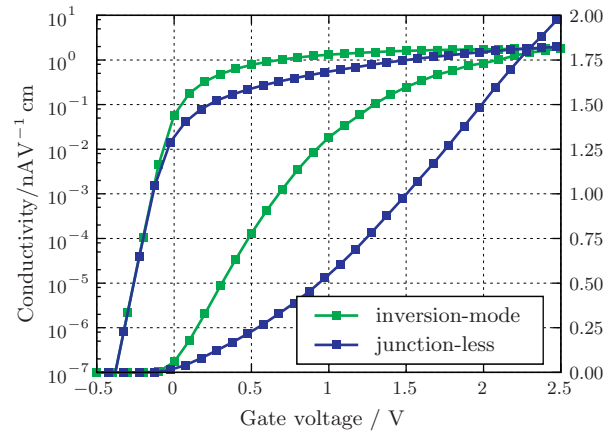


Fig. 17. Trans-conductivity for channels from Fig. 15; gate work-functions have been adjusted so that both the inversion-mode and the junction-less device have the same threshold voltage. In inversion-mode channels the conductivity saturates due to SRS. In junction-less devices conductivity is lower initially but shows no saturation.

of the investigated devices is the n-type FinFET presented in [1]. The cross-section geometry was generated based on a TEM-image of the channel as shown in Fig. 13. We investigated the orientation-dependence of channel conductivity, varying the orientation of both channel and substrate. The result can be seen in Fig. 14. The orientation affects the saturation behavior of the conductivity, an effect which we attribute to SRS [2].

We also investigated the junction-less (JL) FET presented in [3], which has a Π -gate nanowire channel as shown in Fig. 15. The channel of the JL-FET was benchmarked against an inversion-mode device with the same geometry. Fig. 16 shows a breakdown of the various scattering mechanisms' influence on channel mobility and Fig. 17 the trans-conductivity curves. While the JL-FET can reach higher low-field currents than the inversion-mode device, the inversion-mode device has a steeper switching curve. This feature is also visible in the measurements from [3].

6. Conclusion

We presented a versatile and efficient computational toolkit for low-field mobility analysis in nano-scale devices based on physical models. The models were formulated in a dimension-independent manner and provide consistent results between the 2DEG and 1DEG regime of carrier transport. The consistency was confirmed by simulations and the critical length that separates the two regimes was determined.

The presented work enables differential analysis of devices which is crucial in the evaluation of novel device designs. This capability was also demonstrated on two of the most recently realized non-planar devices, the FinFET and the junction-less nanowire FET.

Acknowledgment

This work has been supported by the Austrian Science fund through contracts F025 and I841-N16.

References

- [1] Auth C, Allen C, Blattner A, Bergstrom D, Brazier M, Bost M, et al. A 22 nm high performance and low-power CMOS technology featuring fully-depleted tri-gate transistors, self-aligned contacts and high density MIM capacitors. In: VLSIT; 2012. p. 131–2. <http://dx.doi.org/10.1109/VLSIT.2012.6242496>.

- [2] Stanojevic Z, Karner M, Kosina H. Exploring the design space of non-planar channels: shape, orientation, and strain. In: Intl. electron device meeting; 2013. p. 332–5.
- [3] Colinge J-P, Lee C-W, Afzalain A, Akhavan ND, Yan R, Ferain I, et al. Nanowire transistors without junctions. *Nat Nano* 2010;5(3):225–9. <http://dx.doi.org/10.1038/nnano.2010.15>.
- [4] Stanojevic Z, Kosina H. VSP – a quantum simulator for engineering applications. In: IWCE; 2013. p. 93–4.
- [5] Baumgartner O, Stanojevic Z, Schnass K, Karner M, Kosina H. VSP – a quantum-electronic simulation framework. *J Comput Electron*. <http://dx.doi.org/10.1007/s10825-013-0535-y>.
- [6] GTS Framework. <<http://www.globaltcad.com/en/products/gts-framework.html>> [accessed 02.07.13].
- [7] Stanojevic Z, Karner M, Schnass K, Kernstock C, Baumgartner O, Kosina H. A versatile finite volume simulator for the analysis of electronic properties of nanostructures. In: SISPAD; 2011. p. 143–6. <http://dx.doi.org/10.1109/SISPAD.2011.6035089>.
- [8] Lehoucq R, Sorensen D, Yang C. ARPACK users' guide: solution of large-scale eigenvalue problems with implicitly restarted arnoldi methods; 1998.
- [9] Demmel J, Dongarra J, Ruhe A, van der Vorst H. Templates for the solution of algebraic eigenvalue problems: a practical guide. Society for Industrial and Applied Mathematics, Philadelphia, PA, USA; 2000.
- [10] Kawaji S. The two-dimensional lattice scattering mobility in a semiconductor inversion layer. *J Phys Soc Jpn* 1969;27(4):906–8. <http://dx.doi.org/10.1143/JPSJ.27.906>. arXiv:<http://journals.jps.jp/doi/abs/10.1143/JPSJ.27.906>.
- [11] Ramayya EB, Vasileska D, Goodnick SM, Knezevic I. Electron transport in silicon nanowires: the role of acoustic phonon confinement and surface roughness scattering. *J Appl Phys* 2008;104(6):063711. <http://dx.doi.org/10.1063/1.2977758>. <<http://link.aip.org/link/?JAP/104/063711/1>>.
- [12] Prange RE, Nee T-W. Quantum spectroscopy of the low-field oscillations in the surface impedance. *Phys Rev* 1968;168:779–86. <http://dx.doi.org/10.1103/PhysRev.168.779>.
- [13] Goodnick SM, Ferry DK, Wilmsen CW, Liliental Z, Fathy D, Krivanek OL. Surface roughness at the Si(100)-sio₂ interface. *Phys Rev B* 1985;32:8171–86. <http://dx.doi.org/10.1103/PhysRevB.32.8171>.
- [14] Baumgartner O, Stanojevic Z, Kosina H. Efficient simulation of quantum cascade lasers using the Pauli master equation. In: SISPAD; 2011. p. 91–4. <http://dx.doi.org/10.1109/SISPAD.2011.6035057>.
- [15] Demmel James W, Eisenstat Stanley C, Gilbert John R, Li Xiaoye S, Liu Joseph WH. A supernodal approach to sparse partial pivoting. *SIAM J Matrix Anal Appl* 1999;20(3):720–55.
- [16] Trellakis A, Galick AT, Pacelli A, Ravaoli U. Iteration scheme for the solution of the two-dimensional Schrödinger-Poisson equations in quantum structures. *J Appl Phys* 1997;81(12):7880–4. <http://dx.doi.org/10.1063/1.365396>. <<http://link.aip.org/link/?JAP/81/7880/1>>.
- [17] Jungemann C, Meinerzhagen B. Hierarchical device simulation: the Monte-Carlo perspective. Springer; 2003.
- [18] Herring C, Vogt E. Transport and deformation-potential theory for many-valley semiconductors with anisotropic scattering. *Phys Rev* 1956;101:944–61. <http://dx.doi.org/10.1103/PhysRev.101.944>.